Temperature elevation by HIFU in *ex vivo* porcine muscle: MRI measurement and simulation study

Maxim A. Solovchuk[a)]
Center for Advanced Study in Theoretical Sciences (CASTS), National Taiwan University, Taipei 10617, Taiwan

San Chao Hwang and Hsu Chang
Medical Engineering Research Division, National Health Research Institute, Miaoli 35053, Taiwan

Marc Thiriet
Sorbonne Universités, UPMC Univ Paris 06, UMR 7598, Laboratoire Jacques-Louis Lions, F-75005, Paris, France

Tony W. H. Sheu[b)]
Department of Engineering Science and Ocean Engineering, National Taiwan University, No. 1, Sec. 4, Roosevelt Road, Taipei 10617, Taiwan, Republic of China and Center for Advanced Study in Theoretical Sciences (CASTS), National Taiwan University, Taipei 10617, Taiwan

(Received 2 September 2013; revised 25 March 2014; accepted for publication 26 March 2014; published 18 April 2014)

Purpose: High-intensity focused ultrasound is a rapidly developing medical technology with a large number of potential clinical applications. Computational model can play a pivotal role in the planning and optimization of the treatment based on the patient's image. Nonlinear propagation effects can significantly affect the temperature elevation and should be taken into account. In order to investigate the importance of nonlinear propagation effects, nonlinear Westervelt equation was solved. Weak nonlinear propagation effects were studied. The purpose of this study was to investigate the correlation between the predicted and measured temperature elevations and lesion in a porcine muscle.
Methods: The investigated single-element transducer has a focal length of 12 cm, an aperture of 8 cm, and frequency of 1.08 MHz. Porcine muscle was heated for 30 s by focused ultrasound transducer with an acoustic power in the range of 24–56 W. The theoretical model consists of nonlinear Westervelt equation with relaxation effects being taken into account and Pennes bioheat equation.
Results: Excellent agreement between the measured and simulated temperature rises was found. For peak temperatures above 85–90 °C "preboiling" or cavitation activity appears and lesion distortion starts, causing small discrepancy between the measured and simulated temperature rises. From the measurements and simulations, it was shown that distortion of the lesion was caused by the "preboiling" activity.
Conclusions: The present study demonstrated that for peak temperatures below 85–90 °C numerical simulation results are in excellent agreement with the experimental data in three dimensions. Both temperature rise and lesion size can be well predicted. Due to nonlinear effect the temperature in the focal region can be increased compared with the linear case. The current magnetic resonance imaging (MRI) resolution is not sufficient. Due to the inevitable averaging the measured temperature can be 10–30 °C lower than the peak temperature. Computational fluid dynamics can provide additional important information that is lost using a state of the art MRI device. © *2014 American Association of Physicists in Medicine*. [http://dx.doi.org/10.1118/1.4870965]

Key words: HIFU, Westervelt equation, magnetic resonance guided high intensity focused ultrasound, porcine muscle

1. INTRODUCTION

High intensity focused ultrasound (HIFU) is a rapidly developing medical technology for performing a noninvasive tumor ablation surgery. This therapy has been successfully applied to ablate solid malignant tumors in different organs such as prostate, breast, liver, pancreas, uterine fibroids.[1–3] The absorbed ultrasound energy in tissue is transformed into the thermal energy during focused therapy and this energy deposition can quickly elevate tissue temperature. Subject to the focused ultrasound beam, thermal energy can be added primarily to a small region of tissues with little or no deposition at all on the surrounding tissues. When tissue is heated to a temperature higher than 56 °C for 1 s, thermal coagulation necrosis occurs.[4] However, usually higher temperatures are used (65–85 °C) to ensure complete ablation of cancer cells.[5] At an even higher temperature above 100 °C, tissue may boil, thereby leading to an unpredictable lesion growth[4,6,7] and causing necrosis of healthy tissues.

HIFU therapy is usually performed with magnetic resonance imaging (MRI) or diagnostic US guidance. These two imaging procedures have their own advantages and disadvantages.[1] MRI is the only imaging modality that can measure tissue temperature elevation during focused

ultrasound treatment. The resulting temperature response can help to choose proper acoustic parameters during the treatment and reduce time needed for the treatment planning. However, MRI guidance is expensive and has limitations in spatial and temporal resolutions.[1,8,9] MRI measures spatial and temporal average temperatures, and this can lead to an underestimation of the temperature.[1,8,9] For example, in Ref. 8 the numerical simulation results predicted the peak temperature 100 °C after 7 s heating. Spatial averaging over the voxel volume results in the temperature 73 °C, which agrees well with the measured MRI temperature. The temperatures measured by MRI were underestimated by about 30% due to spatial averaging, which can lead to the errors in the estimation of the thermal dose (TD). US guidance can define tumor location, but it does not give information about tissue temperature and transient lesion monitoring is complicated. The necrosed volume is not very well visible by US imaging so that lesion boundaries cannot be well localized. Gas bubbles are formed in the focal area and this region can be seen as an echogenic region. Treatment planning[10–13] becomes therefore very important for US imaging. Before the treatment acoustic parameters of the transducer should be well adjusted in the case of US guided focused ultrasound therapy. To avoid undesirable damage of healthy tissues, ultrasound beam should be properly focused with a correct amount and precise distribution of the deposited energy.[14] Use of insufficient acoustic power may require repeated treatments or even disease progression.[15–17] For both imaging procedures treatment planning plays an important role. For MRI guided focused ultrasound treatment planning is very important, when nonthermal mechanisms[15] are used in the treatment and temperature monitoring cannot be used as a guidance. A correct choice of mathematical and physical models becomes therefore one of the crucial factors in the planning of therapeutic procedure.

Previously thermocouples were mostly used for the monitoring of temperature and validation of the numerical model.[18] Thermocouple can invasively measure the temperature at just one point. There are several drawbacks associated with the use of thermocouples. First of all, it is difficult to control the position of the thermocouple relative to the ultrasonic beam. Second, the presence of thermocouple can increase the heating rate.[19,20] MRI permits the measurement of two- or three-dimensional temperature distribution that can be used to validate the model and does not have the drawbacks mentioned above. In the present work, MRI temperature measurements have been performed and compared with the numerical simulation results.

At high intensities nonlinear wave propagation effects lead to the distortion of waveform. Because of the nonlinear distortion higher harmonics are generated. These higher harmonics are more readily absorbed by the tissue and can, in turn, improve the local heating. The two most popular nonlinear models chosen for the simulation of focused ultrasound fields are Khokhlov-Zabolotskaya-Kuznetsov (KZK) and Westervelt equations. KZK equation is valid for directional sound beams and can be applied to transducers with the aperture angles smaller than 16°–18°.[21,22] For wide aperture angles, it is better to use the more general Westervelt equation. The transducer in the current study has the aperture angle 19.4°. The nonlinear Westervelt equation is therefore chosen for the simulation carried out in this paper.

Nonlinear propagation effects lead to the enhanced heating.[7] When boiling appears lesion starts to grow toward the transducer.[6] In the current work, we are going to investigate the temperature elevation in a porcine muscle. Both MRI measurement and numerical simulation have been performed. To the best of authors' knowledge, it is the first time when three-dimensional temperature distribution measured by MRI has been compared with the simulation results.

2. MATHEMATICAL MODEL

2.A. Nonlinear acoustic equation

Acoustic field generated by a HIFU source was modeled using the nonlinear Westervelt equation[23–25]

$$\nabla^2 p - \frac{1}{c_0^2}\frac{\partial^2 p}{\partial t^2} + \left[\frac{\delta}{c_0^4} + \frac{2}{c_0^3}\sum_{\nu}\frac{c_\nu \tau_\nu}{1+\tau_\nu \frac{\partial}{\partial t}}\right]\frac{\partial^3 p}{\partial t^3} + \frac{\beta}{\rho_0 c_0^4}\frac{\partial^2 p^2}{\partial t^2} = 0. \quad (1)$$

In the above, p is the sound pressure, $\beta = 1 + \frac{B}{2A}$ is the coefficient of nonlinearity, δ is the diffusivity of sound resulting from fluid viscosity and heat conduction, τ_ν is the relaxation time, and c_ν is the small signal sound speed increment for the νth relaxation process. The first two terms describe the linear lossless wave propagating at a small-signal sound speed. The third term denotes the loss due to thermal conduction and fluid viscosity, and the fourth term accounts for the relaxation processes. The last term denotes acoustic nonlinearity which may considerably affect thermal and mechanical changes within the tissue. Equation (1) can be transformed to the coupled system of two partial differential equations given below[23]

$$\nabla^2 p - \frac{1}{c_0^2}\frac{\partial^2 p}{\partial t^2} + \frac{\delta}{c_0^4}\frac{\partial^3 p}{\partial t^3} + \frac{\beta}{\rho_0 c_0^4}\frac{\partial^2 p^2}{\partial t^2} + \sum_{\nu} P_\nu = 0,$$
$$\left(1 + \tau_\nu \frac{\partial}{\partial t}\right) P_\nu = \frac{2}{c_0^3} c_\nu \tau_\nu \frac{\partial^3 p}{\partial t^3}. \quad (2)$$

In the present paper, two relaxation processes ($\nu = 2$) were considered. Unknown relaxation parameters were calculated by minimizing a mean square error between the linear attenuation law and relaxation model.[23]

For the linear Westervelt equation, the intensity is equal to $I_L = p^2/2\rho c_0$. For the nonlinear case, the total intensity is

$$I = \sum_{n=1}^{\infty} I_n, \quad (3)$$

where I_n are the corresponding intensities for the respective harmonics nf_0. The ultrasound power deposition per unit volume is calculated as follows:

$$q = \sum_{n=1}^{\infty} 2\alpha(nf_0) I_n. \quad (4)$$

The absorption in tissue shown above obeys the following frequency law:

$$\alpha = \alpha_0 \left(\frac{f}{f_0} \right)^{\eta}, \tag{5}$$

where $\alpha_0 = 4.5$ Np/m, $\eta = 1.0$, and $f_0 = 1$ MHz.[27]

2.B. Energy equation for tissue heating

In a region free of large blood vessels, the diffusion-type Pennes bioheat equation[30] given below will be employed to model the transfer of heat in a perfused tissue region

$$\rho_t \, c_t \frac{\partial T}{\partial t} = k_t \nabla^2 T - w_b \, c_b \, (T - T_\infty) + q. \tag{6}$$

In the above energy equation proposed for modeling the time-varying temperature in the tissue domain, ρ, c, k denote the density, specific heat, and thermal conductivity, respectively, with the subscripts t and b referring to the tissue and blood domains. The notation T_∞ is denoted as the temperature at a remote location. In the present study, *ex vivo* porcine muscle is considered and the perfusion rate w_b for the tissue cooling in capillary flow is equal to zero. The above energy equation for T is coupled with the Westervelt equation (1) for the acoustic pressure through a power deposition term q defined in Eq. (4). Initially, we consider that the temperature is equal to 20 °C. On the wall a constant temperature of 20 °C was prescribed. A detailed description of the solution procedures can be found in our previous papers.[17,23]

Thermal dose developed by Sapareto and Dewey[31] will be applied to give us a quantitative relationship between the temperature and time for the tissue heating and the extent of cell killing. In focused ultrasound surgery (generally above 50 °C), the expression for the TD can be written as

$$TD = \int_{t_0}^{t_{\text{final}}} R^{(T-43)} dt \approx \sum_{t_0}^{t_{\text{final}}} R^{(T-43)} \Delta t, \tag{7}$$

where $R = 2$ for $T \geqq 43$ °C, $R = 4$ for 37 °C $< T <$ 43 °C. The value of TD required for a total necrosis ranges from 25 to 240 min in biological tissues.[31,32] According to this relation, thermal dose resulting from heating the tissue to 43 °C for 240 min is equivalent to that achieved by heating the same tissue to 56 °C for 1 s. In the current work, the value of thermal dose equal to 240 min is considered for the prediction of the lesion shape.

3. THREE-POINT SIXTH-ORDER ACCURATE SCHEME FOR WESTERVELT EQUATION

Discretization of the Westervelt equation (1) is started with the approximation of temporal derivatives.[23] Temporal derivatives were approximated by second-order accurate schemes as follows:

$$\left.\frac{\partial^2 p}{\partial t^2}\right|^{n+1} = \frac{2p^{n+1} - 5p^n + 4p^{n-1} - p^{n-2}}{(\Delta t)^2}, \tag{8}$$

$$\left.\frac{\partial^3 p}{\partial t^3}\right|^{n+1} = \frac{6p^{n+1} - 23p^n + 34p^{n-1} - 24p^{n-2} + 8p^{n-3} - p^{n-4}}{2(\Delta t)^3}. \tag{9}$$

The nonlinear term $\frac{\partial^2 p^2}{\partial t^2}|^{n+1}$ is linearized using the second-order accurate relation

$$\begin{aligned}\left.\frac{\partial^2 p^2}{\partial t^2}\right|^{n+1} &= \frac{\partial}{\partial t}\left(\frac{\partial p^2}{\partial t}\right) = 2\frac{\partial}{\partial t}\left(p^n \left.\frac{\partial p}{\partial t}\right|^{n+1} + p^{n+1} \left.\frac{\partial p}{\partial t}\right|^{n} - p^n \left.\frac{\partial p}{\partial t}\right|^{n}\right) \\ &= 2\left(2p_t^n p_t^{n+1} + p^n p_{tt}^{n+1} + p^{n+1} p_{tt}^n - \left(p_t^n\right)^2 - p^n p_{tt}^n\right).\end{aligned} \tag{10}$$

The above two approximation equations are then substituted into Eq. (1) to yield the following inhomogeneous Helmholtz equation:

$$u_{xx} - ku = f(x). \tag{11}$$

Development of a high-order scheme for Helmholtz equation can be constructed by introducing more finite-difference stencil points. The improved prediction accuracy will be, however, at the cost of conducting matrix calculation. To retain the prediction accuracy without an expensive computational cost, we are motivated to develop a scheme that can give us the accuracy order of sixth in a grid stencil involving only three points. To achieve the above goal, the values of $u^{(2)}$, $u^{(4)}$, and $u^{(6)}$ are defined first at a nodal point j as follows:

$$u^{(2)}|_j = s_j, \; u^{(4)}|_j = t_j, \; u^{(6)}|_j = w_j. \tag{12}$$

The proposed compact difference scheme at x_j relates t, s, and w with u as follows:

$$h^6 \delta_0 w_j + h^4 \gamma_0 t_j + h^2 \beta_0 s_j = \alpha_1 u_{j+1} + \alpha_0 u_j + \alpha_{-1} u_{j-1}. \tag{13}$$

Substituting the Taylor-series expansion into Eq. (13) and conducting then a term-by-term comparison of the derivatives, the introduced free parameters are determined as $\alpha_1 = \alpha_{-1} = -1$, $\alpha_0 = 2$, $\beta_0 = -1$, $\gamma_0 = -\frac{1}{12}$, and $\delta_0 = -\frac{1}{360}$.

Since $s_j = k_j u_j + f_j$, the following two expressions for $t_j = (k_j^2 u_j + 2k_{x,j} u_{x,j} + k_{xx,j} u_j + k_j f_j + f_{xx,j})$ and $w_j = (k_j^3 u_j + 7k_j u_j k_{xx,j} + 6k_j u_{x,j} k_{x,j} + 4k_{x,j}^2 u_j + 6k_{xx,j} f_j + 4k_{xxx,j} u_{x,j} + k_{xxxx,j} u_j + 4k_{x,j} f_{x,j} + k_j f_{xx,j} + f_{xxxx,j})$ are resulted. Equation (13) can then be rewritten as

$$\begin{aligned}&\alpha_1 u_{j+1} + \alpha_1 u_{j-1} \\ &\quad + \left[\alpha_0 - \beta_0 h^2 k_j - \gamma_0 h^4 \left(k_j^2 + k_{xx,j}\right) - \delta_0 h^6 \left(k_j^3 + 7k_j k_{xx,j} + +4k_{x,j}^2 + k_{xxxx,j}\right)\right] u_j \\ &= h^2 \beta_0 f_j + h^4 \gamma_0 \left(2k_{x,j} u_{x,j} + k_j f_j + f_{xx,j}\right) + h^6 \delta_0 (k^2 f_j + k f_{xx,j} + f_{xxxx,j}) \\ &\quad + h^6 \delta_0 (6k_j u_{x,j} k_{x,j} + 6k_{xx,j} f_j + 4k_{xxx,j} u_{x,j} + 4k_{x,j} f_{x,j}).\end{aligned} \tag{14}$$

It follows that

$$\left[1-\left(\frac{1}{2h}-\frac{k_{j+1}h}{12}\right)\left(\frac{1}{360}h^6(4k_{xxx,j}+6k_jk_{x,j})+\frac{1}{6}h^4k_{x,j}\right)\right]u_{j+1}$$
$$-\left[2+h^2k_j+\frac{1}{12}h^4\left(k_j^2+k_{xx,j}\right)+\frac{1}{360}h^6\left(k_j^3+4k_{x,j}^2+7k_jk_{xx,j}+k_{xxxx,j}\right)\right]u_j$$
$$+\left[1+\left(\frac{1}{2\,h}-\frac{k_{j-1}\,h}{12}\right)\left(\frac{1}{360}\,h^6(4\,k_{xxx,j}+6\,k_j\,k_{x,j})+\frac{h^4\,k_{x,j}}{6}\right)\right]u_{j-1}$$
$$=\left[h^2+\frac{k_jh^4}{12}+\frac{1}{360}h^6\left(k_j^2+6k_{xx,j}\right)\right]f_j+\frac{1}{90}h^6k_{x,j}f_{x,j}+\left(\frac{1}{360}h^6\,k_j+\frac{1}{12}h^4\right)f_{xx,j}$$
$$+\frac{1}{360}h^6f_{xxxx,j}+\left[\frac{1}{6}\,h^4k_{x,j}+\frac{1}{360}h^6\left(6k_jk_{x,j}+4k_{xxx,j}\right)\right]\cdot\left[-\frac{h}{12}\left(f_{j+1}-f_{j-1}\right)\right]. \quad (15)$$

The corresponding modified equation for Eq. (11) using the currently proposed compact difference scheme can be derived as follows after performing some algebraic manipulation:

$$u_{xx}-ku=f+\left(\frac{h^6}{20160}\right)u^{(8)}+\left(\frac{h^8}{1814400}\right)u^{(10)}$$
$$+\ldots+\mathrm{HOT}, \quad (16)$$

where HOT denotes higher order terms. The above modified equation analysis sheds light that the Helmholtz scheme developed within the three-point stencil framework can yield a spatial accuracy of sixth order.

Axisymmetric sound beam was considered. The Westervelt equation was solved in cylindrical coordinates in conjunction with the alternating direction implicit solution algorithm. Nonreflecting radiation boundary condition was used in the simulation. A sinusoidal waveform was considered to be uniformly distributed over the transducer surface. Accuracy of the numerical solutions has been examined[23] by comparing them with the known analytical and numerical solutions of other authors.[33,34]

4. EXPERIMENTAL METHODS

A home-made MR-guided HIFU system, including HIFU transducer, motion control system, and image processing software, was constructed from basic elements in medical engineering research division of National Health Research Institute.[35] A fixed focus spherical HIFU-transducer (focal length = 12 cm, operating frequency = 1.08 MHz, electroacoustic efficiency = 27.5%) was mounted on a water bag placed above the object to be ablated. The ultrasound power attenuation through the water bag to the ablated object was less than 1.5%.[35] The transducer was mounted on a nonmagnetic device to enable its movement along three axes. The software was written in C and JAVA languages. Our system has all the necessary functions to perform MR-guided HIFU ablation such as the HIFU power control, HIFU transducer positioning, PC to MRI scanner communication, target temperature measurement, and ablated tissue necrosis monitoring.

Temperature measurement was based on the temperature-dependent proton resonance frequency (PRF) shift, which worked well as the targets were abundant of water such as muscle, liver, kindly, etc. The frequency shift can be derived pixel-by-pixel from the phase difference between a reference MRI image (unheated) and a measured MRI image (heated). Thank to our software, the MRI k-space data can be obtained from MRI console to personal computer immediately after the completion of scanning. Afterwards, it was reconstructed to the magnitude image and the phase image. The magnitude image was the ordinary MRI image, which showed the MRI anatomic contrast information, and the phase image was used to calculate the temperature map. The magnitude image and temperature map were fused with gray level and pseudo color, respectively, to identify the hot spot of the ablated tissue. The MRI scanning and the temperature map display were performed continuously during the whole process of focused ultrasound ablation.

In the current study, two MRI scanning sequences, SPoiled GRadient echo (SPGR), and Inversion Recovery Turbo Spin Echo (IR-TSE) were used for different purposes. SPGR was used to get the MRI temperature map such that it was set as fast as possible to get higher temporal resolution for a real time HIFU ablation study. The drawback is that the signal-to-noise ratio (SNR) is lower and the spatial resolution is limited. To improve the signal-to-noise ratio, we set a thick slice thickness (8 mm) and low imaging resolution (2 mm per pixel) for the SPGR sequence. For the temperature measurements along the acoustic axis thinner slice thickness (3 mm) was chosen.

IR-TSE was used for denatured region identification after HIFU ablation was finished. Higher spatial resolution was used for this scanning sequence, the scanning time was therefore longer. We set a thin slice thickness (6 mm), higher resolution (1 mm per pixel), and repeated it twice to obtain the average value for the IR-TSE sequence.

Biological tissue is denatured by heat that changes its magnetic resonance characteristic: longitudinal relaxation time (T1). The IR method was used to distinguish the denatured region from the surrounding area. By setting a specific value of the inversion time (TI), the signal from either the denatured

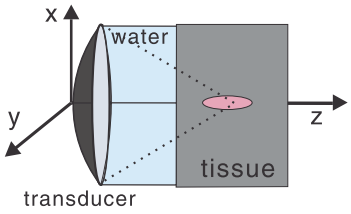

FIG. 1. Schematic of the experiment.

region or from the normal tissue can be eliminated.[35] For example, in Fig. 7, while the inversion time was set as 550 ms, the image of normal porcine meat was almost suppressed and the denatured region was enhanced.

A spoiled gradient echo sequence was chosen in a 1.5 T MRI scanner (Symphony, Siemens) with the following parameters: TR = 13 ms, TE = 7 ms, flip angle = 30°, data matrix 128 × 128, field of view (FOV) = 256 × 256 mm, slice thickness = 8 mm. It took 1.7 s to get one MRI image. After HIFU ablation, the tissue necrosis evaluation was performed with IR-TSE (TR = 3000 ms, TE = 13 ms, TI = 550 ms, average = 2, matrix = 256 × 256, slice thickness = 6 mm).

The HIFU transducer used in this study is a single element that is spherically focused with an aperture of 8 cm and a focal length of 12 cm. The experimental exposure was continuous for 30 s. In this study, the transducer with the frequency $f = 1.08$ MHz was used. The efficiency of the home-made transducer, which is equal to 27.5%, was measured by the radiation force balance method. Electric power of the transducer is varied from 80 to 200 W in our experiment. The measurements have been repeated for three times and the temperature difference was about 5%.

The schematic of the experiment is presented in Fig. 1. The focal point was located at location with the distance 3–3.5 cm below the surface of porcine muscle. We used as fresh as possible a slice of pork. There was a water bag between the slice of pork and the transducer.

5. RESULTS AND DISCUSSION

5.A. Pressure measurements

The transducer was calibrated in water in the following setting. The acoustic source and hydrophone were immersed in filtered and deionized water that is contained in a 74.5-cm-long, 36-cm-wide, and 50-cm-high tank, which is open to the atmosphere. A three-dimensional computerized positioning system is used to move the transducer along the beam axis and orthogonal directions. The transducer was driven by a continuous wave.

In Fig. 2, the measured pressure profiles are plotted against the axial and radial distances (in the focal plane). The solid lines and open circles correspond to the prediction and measurement results, respectively. These results were obtained in water at 25 °C using the chosen 0.4 mm hydrophone (Onda HNA-0400). The efficiency of the employed transducer was measured using the radiation force balance method. The electric energy of the transducer is equal to 1.9 W. The measured acoustic pressures are normalized by the focal pressure of 0.55 MPa. Good agreement between the measured and numerical results can be seen.

5.B. Tissue property measurements

Differences in acoustic and thermal properties of abdominal soft tissues may affect the delivery of thermal energy. Thermal lesions should be created accurately at the certain location without damaging the healthy tissues. The available data on tissue properties have some variations due to different measurement techniques and tissue types. Tissue properties are patient specific and can also vary between tumors and healthy tissues. In order to improve treatment planning, accurate characterization of the physical properties of tissue is required. During the treatment noninvasive methods of estimating thermal conductivity, perfusion and acoustic absorption are necessary.[28,29] In the current work, *ex vivo* study was considered, therefore the perfusion was equal to zero.

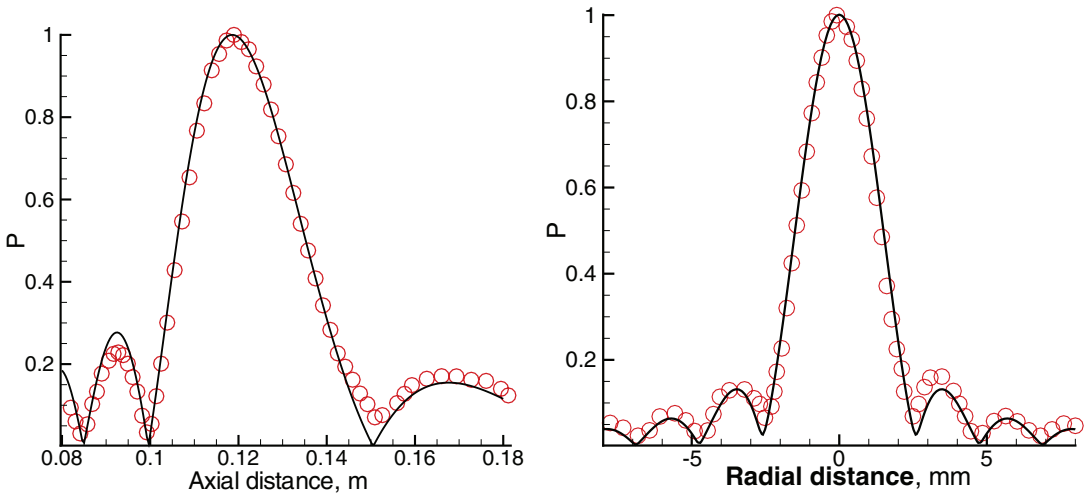

FIG. 2. The measured (circles) and computed (solid line) pressure profiles in water at 1.08 MHz and 0.55 MPa pressure at the focal point.

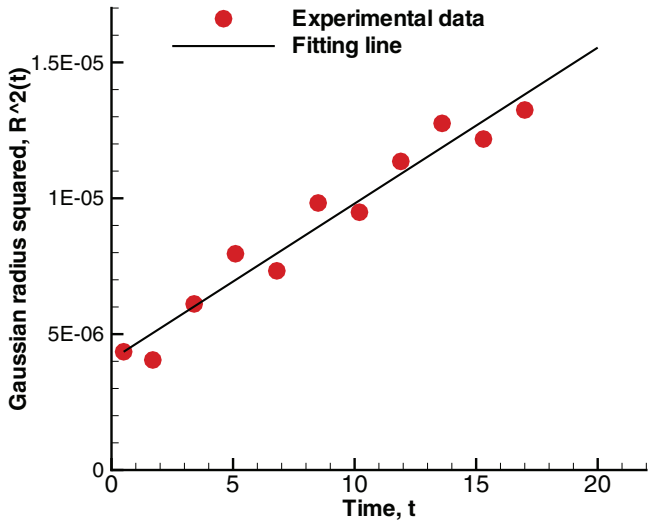

FIG. 3. Measurement of thermal conductivity. Gaussian radius squared $R^2(t)$ is presented as function of time. The slope of the fitting line 5.74×10^{-7} is proportional to the thermal conductivity k_t.

Noninvasive measurements of thermal diffusivity and acoustic absorption have been performed.

The bioheat equation can be rewritten in the form

$$\frac{\partial T}{\partial t} = D\nabla^2 T + Q, \tag{17}$$

TABLE I. Acoustic and thermal properties for the porcine muscle and water.

Tissue	c_0 ($\frac{\text{m}}{\text{s}}$)	ρ ($\frac{\text{kg}}{\text{m}^3}$)	c ($\frac{\text{J}}{\text{kg K}}$)	k ($\frac{\text{W}}{\text{m K}}$)	α ($\frac{\text{Np}}{\text{m}}$)	β
Muscle	1550	1055	3200	0.49	4.5	4.5
Water	1520	1000	4200	0.6	0.026	3.5

where the diffusivity D is equal to $D = k_t/\rho_t c_t$ and $Q = q/\rho_t c_t$. Spatial distribution of focused ultrasound beam energy deposition can be approximated by three-dimensional Gaussian distribution. If we consider a very short heating, immediately after heating the temperature distribution can be fitted as a Gaussian function. This temperature distribution can be considered as an initial temperature. For the measurement of thermal diffusivity, we will analyze the evolution of temperature during the cooling period. In Refs. 28 and 29, it was shown that for a very short heating the solution of the bioheat equation $T(r, z, t)$ at the focal plane $z = z_{\text{focus}}$ can be written in the following form:

$$T(r,t) = A(t)\exp\left(-r^2/\left(2\sigma_{0xy}^2 + 4Dt\right)\right)$$
$$= A(t)\exp(-r^2/R^2(t)),$$

where σ_{0xy} is Gaussian variance in the radial plane at the end of the heating and $R(t)$ is the Gaussian radius. The rate $\partial R^2(t)/\partial t$, at which the Gaussian radius expands, depends only

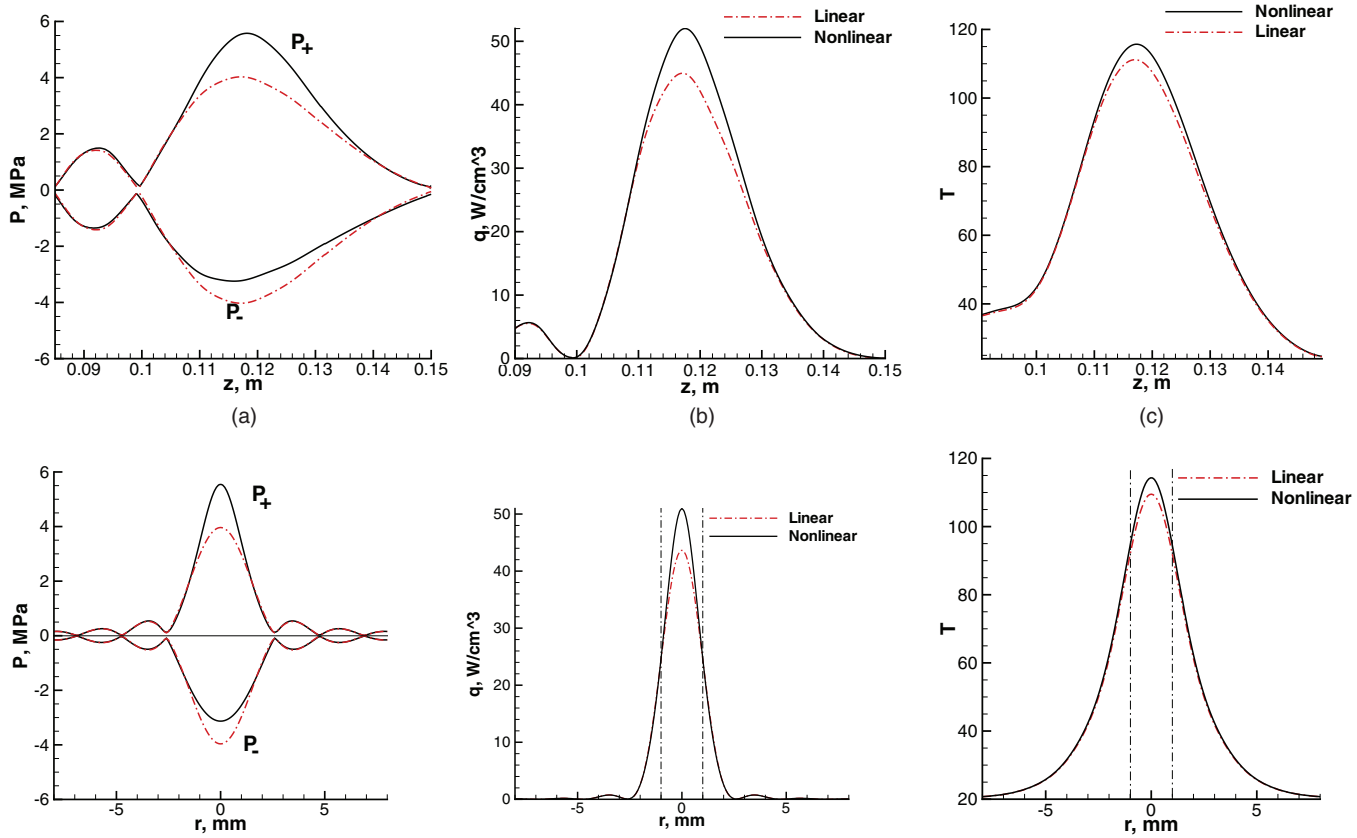

FIG. 4. The simulated linear (dashed-dotted) and nonlinear (solid) pressure (a), power deposition (b), and temperature (c) along the focal axis (upper row) and along the radial axis in the focal plane (lower row) in a slice of pork for the case with electric power 200 W. Dashed-dotted vertical lines indicate the edges of a voxel.

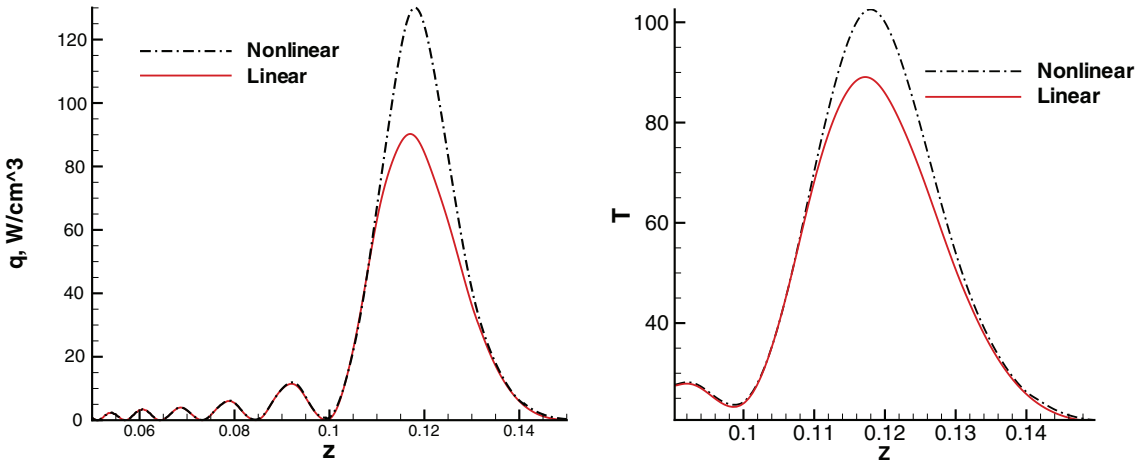

FIG. 5. The simulated linear (solid) and nonlinear (dashed-dotted) power deposition (left) and temperature (right) along the focal axis in the slice of pork for the case with electric power 400 W.

on the thermal diffusivity

$$\frac{\partial R^2(t)}{\partial t} = \frac{\partial}{\partial t}\left(2\sigma_{0xy}^2 + 4Dt\right) = 4D = \frac{4k_t}{\rho_t c_t}. \quad (18)$$

To measure thermal conductivity, we will analyze the evolution of temperature spreading during the cooling period. In our experiment, the tissue was heated for 2 s. Afterwards, the Gaussian radius was measured during the cooling period. In Fig. 3, the Gaussian radius squared is presented as function of time. The slope of the fitting line is $m = 5.74 \times 10^{-7}$. The thermal conductivity is calculated as $k_t = m\rho_t c_t/4 = 0.49$ W/m °C.

The assumptions used in this study for the measurements of thermal conductivity are as follows: (1) tissue is considered to be homogeneous; (2) heating was very fast; (3) tissue properties (density, specific heat, thermal diffusivity) were considered to be constant.

Speed of sound and attenuation coefficient were measured[26] in porcine muscle prior to MRI temperature measurements. The measured speed of sound is 1550 m/s, which agrees with the data of other authors.[27] For the measurement of absorption, we used the method proposed in Ref. 36. Tissue properties used in the current simulation are listed in Table I.[27]

5.C. Importance of acoustic nonlinearity effect

Figure 4 summarizes the results for linear and nonlinear simulations carried out at different acoustic parameters and temperatures in a slice of fresh pork. Acoustic pressure (a), power deposition (b), and temperature (c) are presented along the focal axis (upper row) and along the radial axis (bottom row) for the electric power 200 W. A full-width half pressure maximum of the investigated transducer is 3 mm in the radial direction and 3 cm along the focal axis for the linear acoustic equation.

The peak positive and negative pressures are 5.6 and 3.2 MPa, correspondingly. The peak negative pressure 3.2 MPa lies below the cavitation threshold in a pork muscle.[37,38] In Fig. 4(b), the peak power deposition has been increased by an amount of 16% from the linear to nonlinear waveform. Nonlinear effects are found to be important only in a small region of the focal area. Nonlinear simulation results shown in Fig. 4(c) indicate the peak temperature 115 °C, while the linear theory predicts only 109 °C. These simulated results show that nonlinear propagation effect can enhance heating in the focal zone. In the present work, not very high powers were considered, so the difference between the

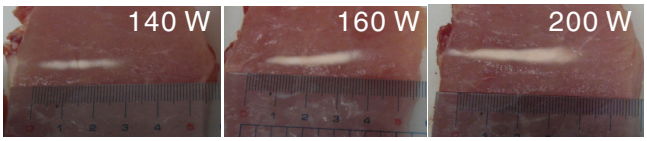

FIG. 6. Lesions (white area) formed in a slice of pork for different electric powers: (a) 140, (b) 160, (c) 200 W. The transducer is located on the right side of the investigated pork slice.

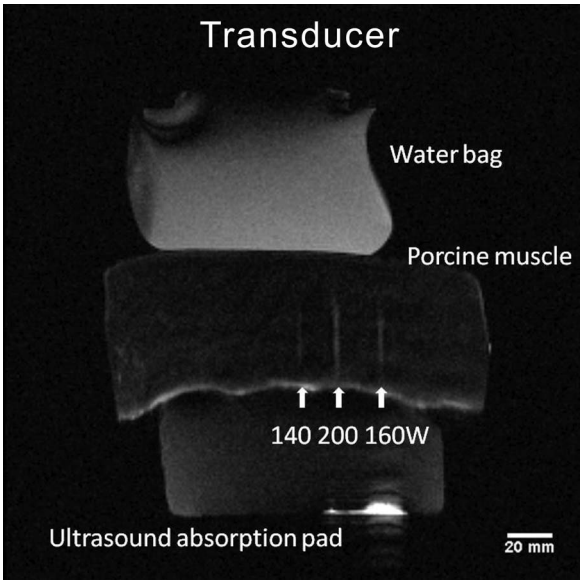

FIG. 7. MRI image of lesions (in white) in porcine muscle for different electric powers: 140, 160, 200 W.

TABLE II. The predicted and measured lesion diameters and lesion lengths at different electric powers.

Power	Simulation (mm)	Visual observation in pork (mm)	MRI image (mm)
140 W, length	23	24	21
140 W, diameter	3	3	2
160 W, length	28	31	25
160 W, diameter	3.4	3	3

predicted linear and nonlinear temperature rises is about 7%. Although both linear and nonlinear theories predict temperatures above 100 °C, nonlinear theory predicts "boiling" that appears in a shorter time (18 s) in comparison with the linear theory (22 s). When tissue temperature reaches 100 °C, vapor/gas bubbles, produced in the focal zone, can reflect and scatter the ultrasound beam, thereby complicating considerably the situation. The echogenic region in the focal area appears and the lesion starts growing toward the transducer, thereby producing a tadpole shape.[6,7,32] It was assumed that before boiling the lesion grew almost symmetrically about the focus and the lesion shape could be well predicted. Neglecting the nonlinear effects in the treatment planning will lead to 4 s underestimation of the "boiling" time. This underestimation can lead to an undesirable damage of healthy tissues in front of the focal region and insufficient ablation of tumor cells behind the focal region. For higher acoustic powers, the effect of acoustic nonlinearity will be larger. For 400 W of electric power (112 W of acoustic power), the peak power deposition is increased by an amount of 45% from linear to nonlinear waveform (Fig. 5). The difference between linear (89 °C) and nonlinear (103 °C) theories for the simulated peak temperatures will be 20%. Dashed-dotted vertical lines in Figs. 4(b) and 4(c) show the width of a voxel, which is 2 mm. The width of a voxel is comparable with the full-width half pressure maximum of the transducer (3 mm). Because MRI measures volume average temperature in a voxel, such a measured temperature will be lower than the peak temperature. In Figs. 4(b) and 4(c), the boundaries of the voxel are presented for a case when the focal point is located at the center of the voxel. However, the focal point can be located anywhere in the voxel. Depending on the focal point location the measured temperature can be quite different. For clinical doctors, the information about the difference between the measured and peak temperatures is of high importance. We will therefore discuss this important issue later in more details. Our emphasis is to show how large the difference can be between the measured and peak temperatures at different locations of the focal point in the voxel.

5.D. MRI measurements and simulation results

In Fig. 6, the lesion shape is presented in a slice of fresh pork under different electric powers. The transducer was located on the right side of the investigated pork slice. In Fig. 7, MRI lesion image is presented. For the case of 80 W, no lesion was observed during the sonication. At the electric power 140 W, the lesion has an ellipsoidal shape. In Table II, we can see that the lesion predicted from the MRI image is smaller than the real lesion in the pork slice due to the limitations in the spatial resolution of MRI image. The lesion predicted from the MRI image is also smaller than the lesion predicted from simulation. There is a good agreement between the simulated and measured lesion widths and lengths for 140 W. For 160 W, only a small disagreement is seen between the simulated and measured lesion sizes. At 160 W, the lesion shape is slightly distorted from the ellipsoidal shape. A mild disagreement between the simulated and measured lesion lengths can be seen. At 200 W, the lesion becomes different from the ellipsoidal shape in the sense that lesion starts to grow toward the transducer and has a "cone" shape. Peak negative pressure at 200 W is 3.2 MPa, which is below the cavitation threshold in the pork muscle. Distortion of the lesion from an ellipsoidal shape cannot be explained any longer by the cavitation activity. Growth of the lesion toward the transducer was attributed mainly to boiling.[6,7] At temperatures above 100 °C boiling

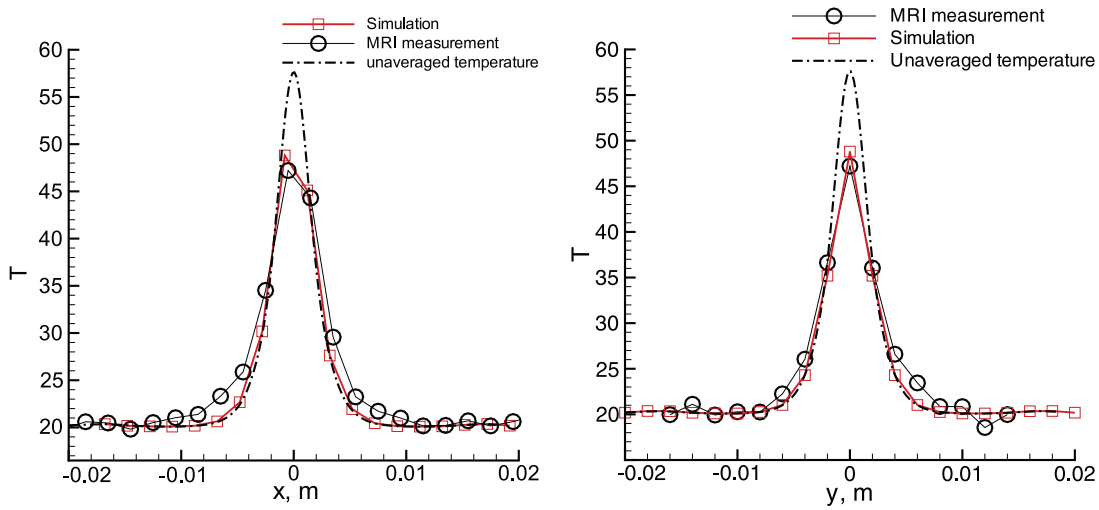

FIG. 8. The measured and computed volume-averaged temperature profiles in porcine muscle at 80 W in the plane perpendicular to the acoustic axis at the focal point at the end of sonication ($t = 30$ s).

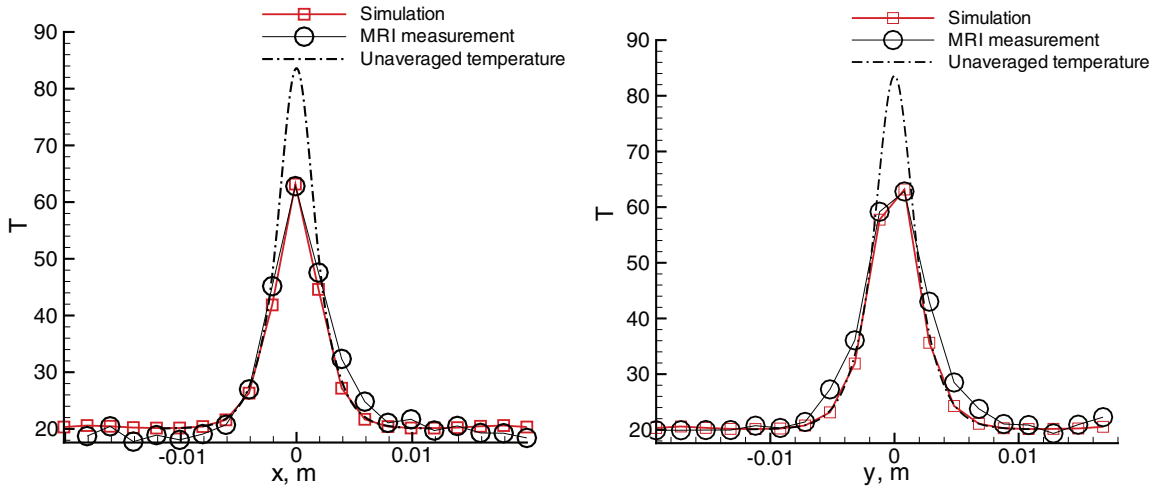

FIG. 9. The measured and computed volume-averaged temperature profiles in porcine muscle at 140 W in the plane perpendicular to the acoustic axis at the focal point at the end of sonication ($t = 30$ s).

in tissues appears. Prior to tissue boiling the lesion has been found to grow almost symmetrically about the focus and the lesion shape can be well predicted. Gas bubbles produced in the focal zone can reflect and scatter ultrasound beam, thereby complicating further the situation. The echogenic region in the focal area appears and the lesion starts to grow toward the transducer.

To compare the simulation and experimental results, it is necessary to average the predicted temperature over the volume of each voxel. The location of focal point inside the voxel is unknown. In the experiment, temperature distribution in the plane perpendicular to the acoustic axis at the focal point was measured. We calculated the volume average temperatures along x and y axes. The calculated temperature profiles were then compared with the experimental results. Afterwards, the location of the focal point inside the voxel was found. Figures 8 and 9 plot the measured and computed volume average temperature profiles in porcine muscle at 80 and 140 W in the plane perpendicular to the acoustic axis at the focal point at the end of sonication ($t = 30$ s). An excellent agreement can be observed between the predicted and simulated data along both x and y axes. In Fig. 10, a good agreement can also be observed between the predicted and simulated data along the acoustic axis z. There is a good agreement between the predicted and simulated temperatures along all three axes. In Fig. 11, the measured and computed volume average 2D temperature contours at 80 W are presented in the plane perpendicular to the acoustic axis at the focal point at the end of sonication ($t = 30$ s). Good agreement can be seen between the predicted and measured data.

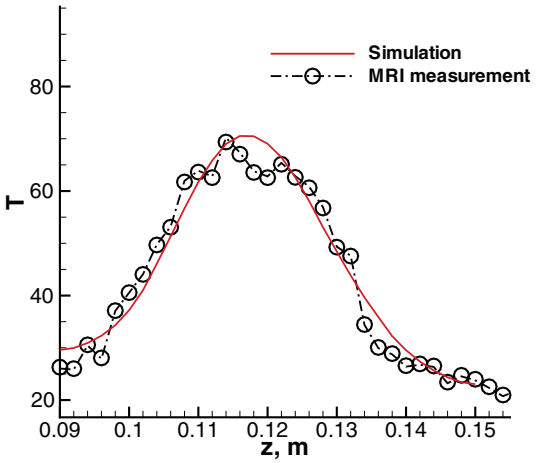

FIG. 10. The measured and computed volume-averaged temperature profiles in porcine muscle at 140 W along the acoustic axis ($t = 30$ s).

In Fig. 12, the predicted temperature contours at $t = 30$ s are presented in the single voxel at the cross-section passing through the focal point for an electric power 140 W for different focal point locations inside the voxel. The predicted peak temperature is 84 °C. Simulations show that depending on the location of the focal point in the voxel the measured peak spatial average temperature can be in the range from 60 °C [Fig. 12(b), focal point at the edge of the voxel] to 75 °C [Fig. 12(a), focal point in the center of voxel]. The real location of the focal point in Fig. 12(c) is shifted by $\Delta y = 0.8$ mm and $\Delta x = 0.1$ mm from the voxel center. The measured spatial average temperature in the voxel is 66 °C. Due to the indispensable averaging, the measured temperature is 9–24 °C lower than the peak temperature depending on where the focal point location is in the voxel. Doctors should keep this finding in mind during the treatment. In Ref. 8, the experimental equipment was adjusted in such a way that focal point was always located at the center of the voxel and it was no need to find the location of the focal point. The authors in Ref. 8 found 27 °C difference between the predicted temperature (100 °C) and the temperature measured by MRI (73 °C). However, during the HIFU surgery with MRI guidance focal point can be located arbitrarily inside the voxel and this can affect the difference between the measured and predicted temperature. For peak temperatures up to 100 °C the measured temperature can be 10–30 °C lower than the peak temperature. This difference also depends on transducer parameters and the size of MRI voxel. Decrease of the size of MRI voxel will decrease the difference between the peak temperature and measured temperature.

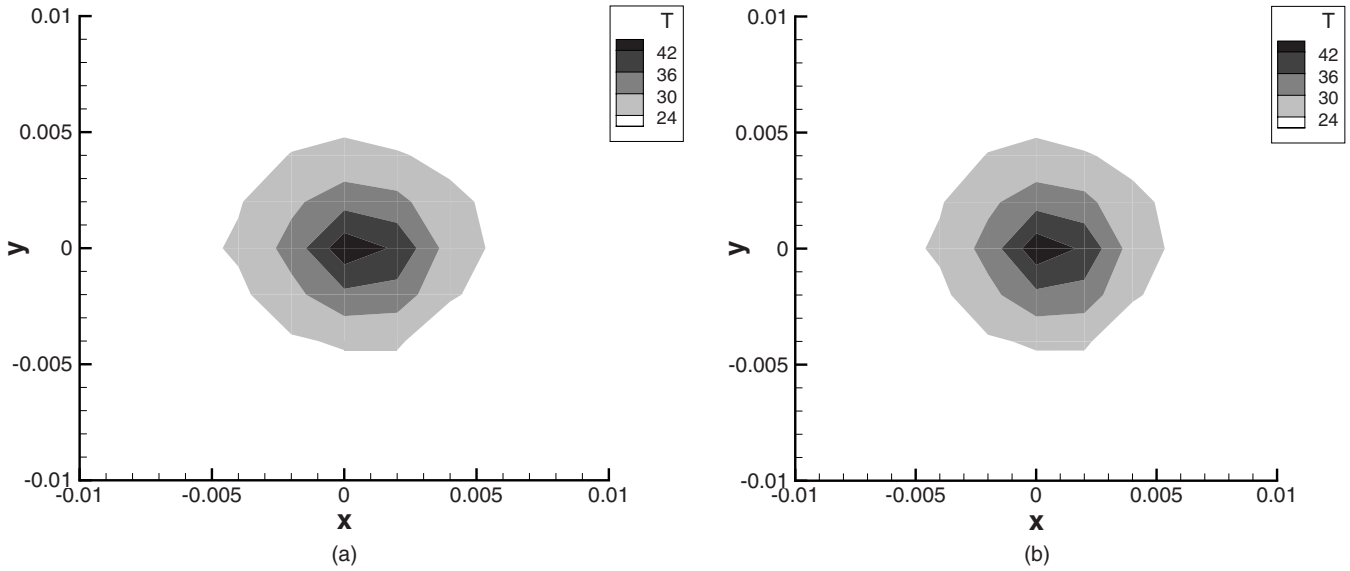

FIG. 11. The measured (a) and simulated (b) volume-averaged temperature contours in porcine muscle at 80 W at the plane perpendicular to the acoustic axis at the focal point at the end of sonication ($t = 30$ s).

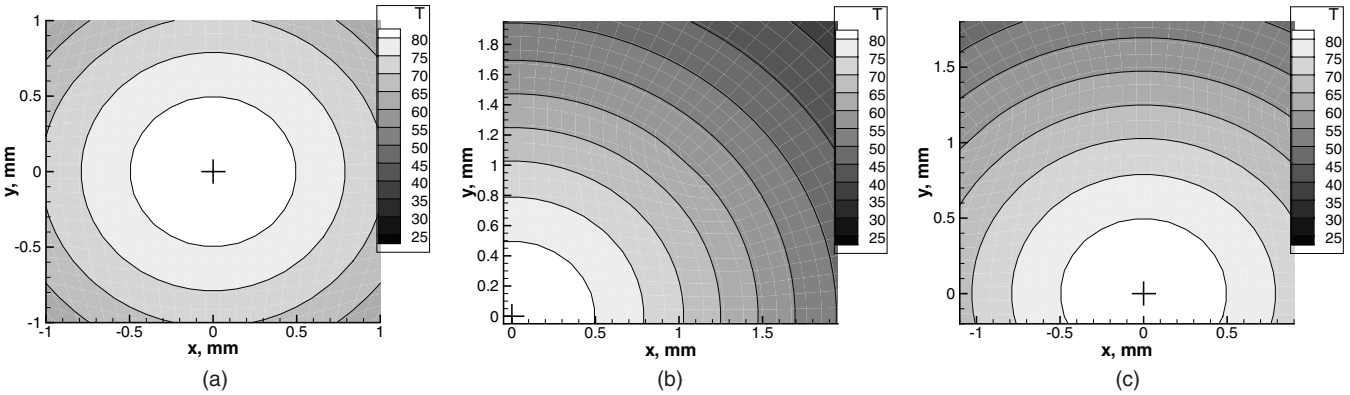

FIG. 12. The simulated temperature contours at $t = 30$ s in a single voxel in the cross-section at the focal point for an electric power 140 W for different focal point locations inside the voxel. Cross (+) denotes the focal point. (a) Focal point is in the center of the voxel, the simulated spatial average temperature in the voxel is $T_{AVG} = 75\,^{\circ}$C. (b) Focal point is close to the edge of the voxel, the simulated spatial average temperature in the voxel is $T_{AVG} = 60\,^{\circ}$C. (c) Real focal point location, $T_{AVG} = 66\,^{\circ}$C.

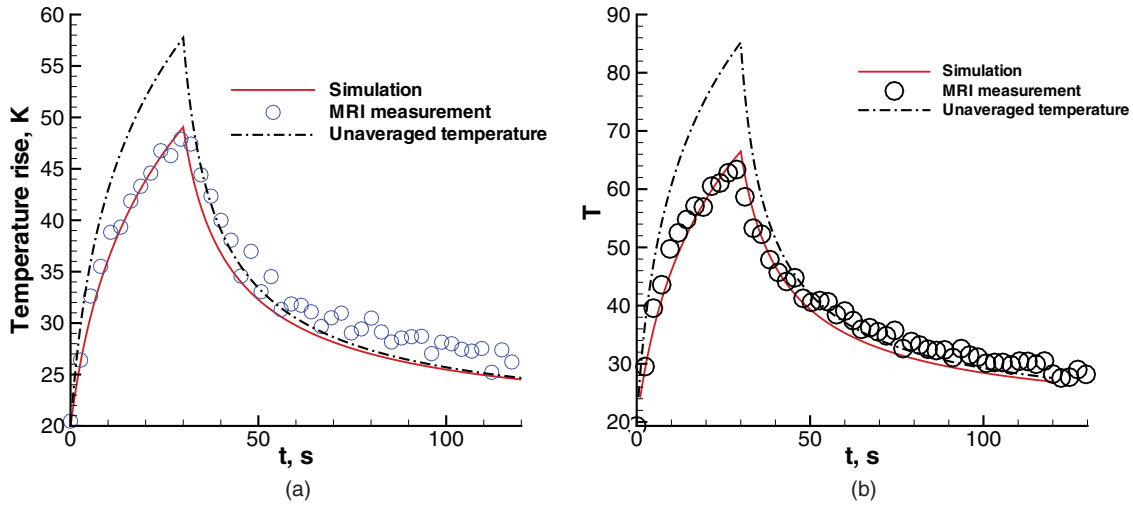

FIG. 13. The measured and computed volume-averaged temperature profiles as function of time in porcine muscle at electric powers (a) 80 and (b) 140 W at the focal point for a 30 s sonication.

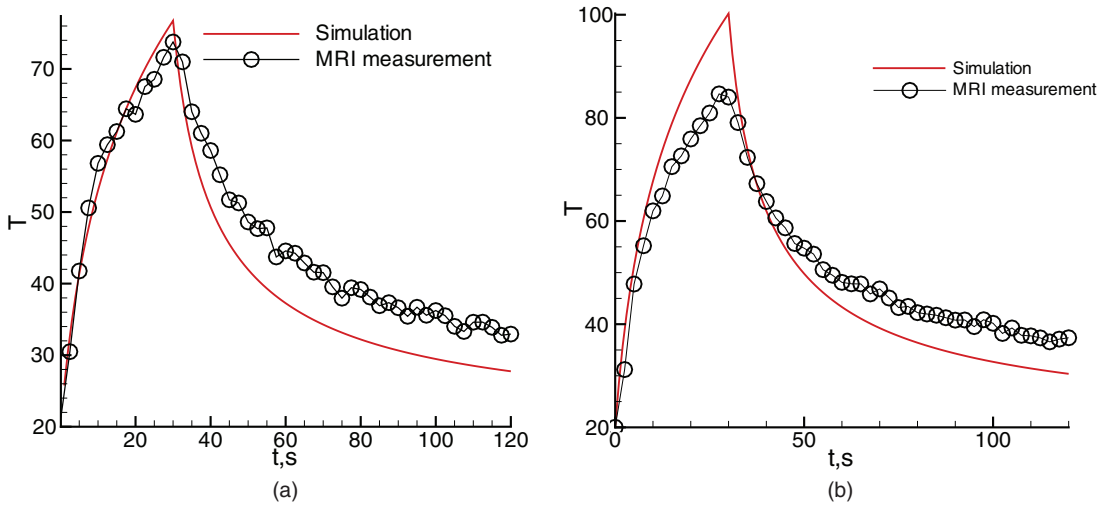

FIG. 14. The measured and computed volume-averaged temperature profiles as function of time in porcine muscle at different electric powers (a) 160 and (b) 200 W at the focus for a 30 s sonication.

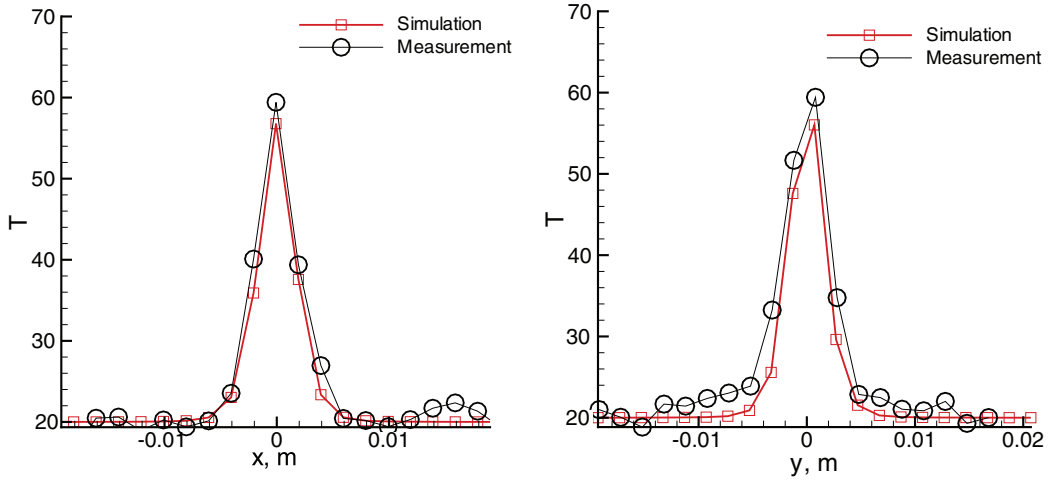

FIG. 15. The measured and computed volume-averaged temperature profiles in porcine muscle at 160 W in the cross-section at the focal point, $t = 12.5$ s.

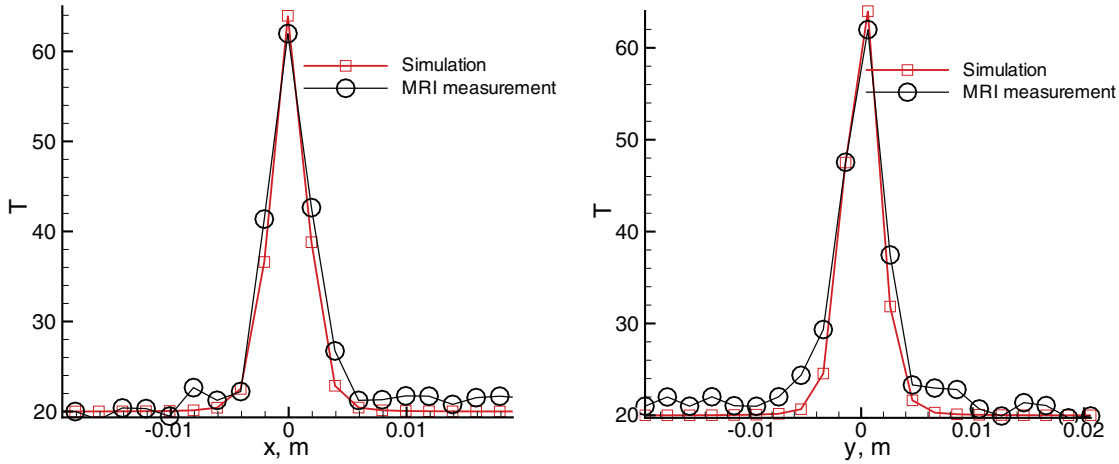

FIG. 16. The measured and computed volume-averaged temperature profiles in porcine muscle at 200 W in the cross-section at the focal point, $t = 10$ s.

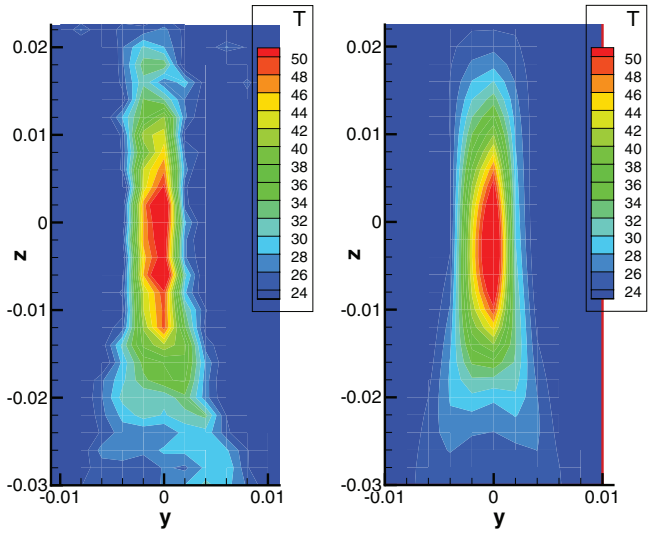

FIG. 17. The measured (left) and computed (right) volume-averaged temperature profiles in porcine muscle at 160 W at the plane parallel to the acoustic axis, $t = 10$ s.

In Fig. 13, we present the measured and computed volume average temperature profiles at electric powers 80 and 140 W as functions of time in porcine muscle at focus. We can see the excellent agreement between the experimental and simulation data for both powers.

In Fig. 14, the measured and computed volume average temperature profiles for electric powers 160 and 200 W are presented. For spatial average temperatures below 70 °C, our simulated results plotted in Figs. 14–16 have excellent agreement with the experimental data. Our two-dimensional simulation results at the cutting plane along acoustic axis in Fig. 17 are in a good agreement with the experimental data. For MRI temperatures above 70 °C, only a small discrepancy can be seen. The measured average temperature 70 °C corresponds to the peak temperature at the focal point in the range of 85–90 °C. For the electric power 160 W at the end of the sonication ($t = 30$ s), the predicted and measured peak temperatures are about 90 °C. In Fig. 6, we can see that for electric power 160 W the lesion is slightly distorted and there is a small disagreement between the predicted and measured lesion lengths. For a peak temperature above 85–90 °C "preboiling" or cavitation activity appears. Peak negative pressure at 200 W is 3 MPa, which is below the cavitation threshold in the tissue.[37] However, at such a high temperature there is a large vapor pressure. Therefore, we can conclude that at a large peak negative pressure boiling will appear at a lower temperature (we will call it "preboiling"). Previously, 100 °C temperature was considered as a threshold value for a lesion to distort. After the current study, we believe that at a time when the temperature reaches 85–90 °C lesion can start growing toward the transducer.

6. CONCLUSION

Temperature elevation in a slice of fresh pork was investigated both experimentally and theoretically. Spatial and temporal resolutions of the MRI thermometry were designed to be close to the resolution used in the clinical practice. It has been shown that nonlinear propagation effect can enhance heating and boiling. There is an excellent agreement between the measured and simulated temperature rise. For peak temperatures above 85–90 °C, "preboiling" or cavitation activity appears and lesion distortion starts and we get only a small discrepancy between the simulated and measured results. From the measurements and simulations, it was shown that distortion of the lesion was caused by the preboiling event. Several mathematical models[39] are available for the analysis of temperature elevation and lesion evolution during thermal therapy. For the current mathematical model, excellent agreement between the theory and experimental data for the temperature rise and lesion size was found for all the studied power levels for peak temperatures below 85–90 °C. The current numerical model is applicable to the case while the peak temperature is below 85–90 °C. At higher temperatures, it is necessary to take into account the effects of boiling and cavitation. MRI measures volume average temperature. Because of the indispensable averaging procedure, the measured temperature can be 10–30 °C lower (depending on the focal point location inside the voxel) than the peak temperature. The measured temperature 70–90 °C may, for example, correspond to the peak temperature 100 °C. This finding should be taken into account during the treatment. The current MRI resolution is not sufficient and computational fluid dynamics is therefore a useful tool to provide additional important information that is lost using a state of the art MRI device.

ACKNOWLEDGMENTS

The authors would like to acknowledge the financial support from the Center for Advanced Study in Theoretical Sciences (CASTS) and from the National Science Council of Republic of China under Contract No. NSC102-2811-M-002-125. The authors also would like to thank Dr. I. Kuo from National Health Research Institutes, Taiwan, for his assistance to set up pressure measurements and perform sound speed measurement.

[a]Electronic mail: solovchuk@gmail.com
[b]Electronic mail: twhsheu@ntu.edu.tw

[1]Y. F. Zhou, "High intensity focused ultrasound in clinical tumor ablation," World J. Clin. Oncol. **2**, 8–27 (2011).
[2]T. A. Leslie and J. E. Kennedy, "High intensity focused ultrasound in the treatment of abdominal and gynaecological diseases," Int. J. Hypertherm. **23**, 173–182 (2007).
[3]O. Al-Bataineha, J. Jenneb, and P. Huberb, "Clinical and future applications of high intensity focused ultrasound in cancer," Cancer Treatment Rev. **38**, 346–353 (2012).
[4]N. T. Wright and J. D. Humphrey, "Denaturation of collagen via heating: An irreversible rate process," Annu. Rev. Biomed. Eng. **4**, 109–128 (2002).
[5]A. Napoli, M. Anzidei, F. Ciolina, E. Marotta, B. C. Marincola, G. Brachetti, L. D. Mare, G. Cartocci, F. Boni, V. Noce, L. Bertaccini, and C. Catalano, "MR-guided high-intensity focused ultrasound: Current status of an emerging technology," Cardiovasc. Interv. Radiol. **36**, 1190–1203 (2013).
[6]W. S. Chen, C. Lafon, T. J. Matula, S. Vaezy, and L. A. Crum, "Mechanisms of lesion formation in high intensity focused ultrasound therapy," Acoust. Res. Lett. Online **4**, 41–46 (2003).

[7]V. A. Khokhlova, M. R. Bailey, J. A. Reed, B. W. Cunitz, P. J. Kaczkowski, and L. A. Crum, "Effects of nonlinear propagation, cavitation and boiling in lesion formation by high intensity focused ultrasound in a gel phantom," J. Acoust. Soc. Am. **119**, 1834–1848 (2006).
[8]T. D. Khokhlova, M. S. Canney, D. Lee, K. I. Marro, L. A. Crum, V. A. Khokhlova, and M. R. Bailey, "Magnetic resonance imaging of boiling induced by high intensity focused ultrasound," J. Acoust. Soc. Am. **125**, 2420–2431 (2009).
[9]S. D. Sokka, R. King, and K. Hynynen, "MRI-guided gas bubble enhanced ultrasound heating in *in vivo* rabbit thigh," Phys. Med. Biol. **48**, 223–241 (2003).
[10]M. A. Solovchuk, T. W. H. Sheu, and M. Thiriet, "Effects of acoustic nonlinearity and blood flow cooling during HIFU treatment," AIP Conf. Proc. **1503**, 83–88 (2012).
[11]M. A. Solovchuk, T. W. H. Sheu, and M. Thiriet, "Image-based computational model for focused ultrasound ablation of liver tumor," J. Comput. Surg. **1**, 4 (13pp.) (2014).
[12]A. Pulkkinen and K. Hynynen, "Computational aspects in high intensity ultrasonic surgery planning," Comput. Med. Imaging Graph. **34**, 69–78 (2010).
[13]T. W. H. Sheu, M. A. Solovchuk, A. W. J. Chen, and M. Thiriet, "On an acoustics-thermal-fluid coupling model for the prediction of temperature elevation in liver tumor," Int. J. Heat Mass Transfer **54**, 4117–4126 (2011).
[14]T. Yu and J. Luo, "Adverse events of extracorporeal ultrasound guided high intensity focused ultrasound therapy," PLoS ONE **6**, e26110 (2011).
[15]D. Schlesinger, S. Benedict, C. Duederich, A. Klibanov, and J. Larner, "MRI-guided focused ultrasound surgery, present and future," Med. Phys. **40**, 080901 (32pp.) (2013).
[16]M. A. Solovchuk, T. W. H. Sheu, W. L. Lin, I. Kuo, and M. Thiriet, "Simulation study on acoustic streaming and convective cooling in blood vessels during a high-intensity focused ultrasound thermal ablation," Int. J. Heat Mass Transfer **55**, 1261–1270 (2012).
[17]M. A. Solovchuk, T. W. H. Sheu, M. Thiriet, and W. L. Lin, "On a computational study for investigating acoustic streaming and heating during focused ultrasound ablation of liver tumor," J. Appl. Therm. Eng. **56**(1–2), 62–76 (2013).
[18]S. Maruvada, Y. Liu, W. F. Pritchard, B. A. Herman, and G. R. Harris, "Comparative study of temperature measurements in *ex vivo* swine muscle and a tissue-mimicking material during high intensity focused ultrasound exposures," Phys. Med. Biol. **57**(1), 1–19 (2012).
[19]J. Huang, R. G. Holt, R. O. Cleveland, and R. A. Roy, "Experimental validation of a tractable medical model for focused ultrasound heating in flow-through tissue phantoms," J. Acoust. Soc. Am. **116**, 2451–2458 (2004).
[20]R. L. Clarke and G. R. ter Haar, "Temperature rise recorded during lesion formation by high-intensity focused ultrasound," Ultrasound Med. Biol. **23**, 299–306 (1997).
[21]J. N. Tjotta, S. Tjotta, and E. H. Vefring, "Effects of focusing on the nonlinear interaction between two collinear finite amplitude sound beams," J. Acoust. Soc. Am. **89**, 1017–1027 (1991).
[22]J. E. Soneson, "A parametric study of error in the parabolic approximation of focused axisymmetric ultrasound beams," J. Acoust. Soc. Am. **131**, EL481–EL485 (2012).
[23]M. A. Solovchuk, T. W. H. Sheu, and M. Thiriet, "Simulation of nonlinear Westervelt equation for the investigation of acoustic streaming and nonlinear propagation effects," J. Acoust. Soc. Am. **134**(5), 3931–3942 (2013).
[24]M. F. Hamilton and C. L. Morfey, "Model equations," in *Nonlinear Acoustics*, edited by M. F. Hamilton and D. T. Blackstock (Academic, Boston, 1998), Chap. 3.
[25]Y. Jing and R. O. Cleveland, "Modeling the propagation of nonlinear three-dimensional acoustics beams in inhomogeneous media," J. Acoust. Soc. Am. **122**, 1352–1364 (2007).
[26]I. Y. Kuo and K. K. Shung, "A novel method for the measurement of acoustic speed," J. Acoust. Soc. Am. **88**, 1679–1682 (1990).
[27]F. A. Duck, *Physical Property of Tissues - A Comprehensive Reference Book* (Academic, London, 1990), p. 346.
[28]H. L. Cheng and D. B. Plewes, "Tissue thermal conductivity by magnetic resonance thermometry and focused ultrasound heating," J. Magn. Reson. Imaging **16**(5), 598–609 (2002).
[29]J. Zhang, C. Mougenot, A. Partanen, R. Muthupillai, and P. H. Hor, "Volumetric MRI-guided high-intensity focused ultrasound for noninvasive, *in vivo* determination of tissue thermal conductivity: Initial experience in a pig model," J. Magn. Reson. Imaging **37**(4), 950–957 (2013).
[30]H. H. Pennes, "Analysis of tissue and arterial blood temperature in the resting human forearm," J. Appl. Physiol. **1**, 93–122 (1948).
[31]S. A. Sapareto and W. C. Dewey, "Thermal dose determination in cancer therapy," Int. J. Radiat. Oncol., Biol., Phys. **10**, 787–800 (1984).
[32]P. M. Meaney, M. D. Cahill, and G. R. ter Haar, "The intensity dependence of lesion position shift during focused ultrasound surgery," Ultrasound Med. Biol. **26**, 441–450 (2000).
[33]D. T. Blackstock, "Connection between the Fay and Fubini solutions for plane sound waves of finite amplitude," J. Acoust. Soc. Am. **39**, 1019–1026 (1966).
[34]H. T. O'Neil, "Theory of focusing radiators," J. Acoust. Soc. Am. **21**(5), 516–526 (1949).
[35]S. C. Hwang, C. Yao, I. Y. Kuo, W. C. Tsai, and H. Chang, "Tissue necrosis monitoring for HIFU ablation with T1 contrast MRI imaging," AIP Conf. Proc. **1359**, 157–162 (2011).
[36]U. Vyas, A. Payne, N. Todd, D. L. Parker, R. B. Roemer, and D. A. Christensen, "Non-invasive patient-specific acoustic property estimation for MR-guided focused ultrasound surgery," AIP Conf. Proc. **1481**, 419–425 (2012).
[37]K. Hynynen, "The threshold for thermally significant cavitation in dog's thigh muscle *in vivo*," Ultrasound Med. Biol. **17**, 157–169 (1991).
[38]T. Li, H. Chen, T. Khokhlova, Y. N. Wang, W. Kreider, X. He, and J. H. Hwang, "Passive cavitation detection during pulsed HIFU exposures of *ex vivo* tissues and *in vivo* mouse pancreatic tumors," Ultrasound Med. Biol. (in press).
[39]S. J. Payne, T. Peng, and D. P. O'Neill, "Mathematical modeling of thermal ablation," Crit. Rev. Biomed. Eng. **38**(1), 21–30 (2010).